

A novel reverberation mapping method for blazars

JUNHAO DENG ,^{1,2} LIZHI LIU,^{1,2} YIFAN WANG ,³ AND YUNGUO JIANG ,^{1,2}

¹*Shandong Provincial Key Laboratory of Optical Astronomy and Solar-Terrestrial Environment, Institute of Space Sciences, Shandong University, Weihai, 264209, People's Republic of China*

²*School of Space Science and Technology, Shandong University, Weihai 264209, People's Republic of China*

³*College of Physics and Electronic Information, Dezhou University, Dezhou 253023, People's Republic of China*

ABSTRACT

Reverberation mapping (RM) is the most promising method to measure the masses of supermassive black holes in the center of active galaxy nuclei (AGNs). However, the dominant jet component hinders the application of RM method for blazars. In this work, we present a new algorithm to disentangle the contribution of the accretion disk from that of the relativistic jet in blazars by analyzing the spectral break of the optical spectroscopic data. We applied this method to two flat-spectrum radio quasars (FSRQs), PKS 1510-089 and PKS 0736+017. In PKS 1510-089, the variability of the H γ line is delayed with respect to the disk emission by approximately 94 days, while the H β line shows a lag of about 111 days relative to the disk. In PKS 0736+017, the H γ variability is delayed with respect to the disk by roughly 66 days, and the H β line exhibits a lag of about 67 days. Based on these measured time lags, we estimate black hole masses of $\sim 1.4 \times 10^8 M_\odot$ for PKS 1510-089 and $\sim 8.1 \times 10^7 M_\odot$ for PKS 0736+017. This method paves the way to apply the RM method for blazars, and improves the understanding of disk and jet activities.

Keywords: Active galactic nuclei (16); Blazars (164); Supermassive black holes (1663)

1. INTRODUCTION

Active galactic nuclei (AGNs) are among the brightest objects in the universe, and have a supermassive black hole (SMBH) at their centers. The accretion process of SMBH leads to distinct radiative structural components, including the accretion disk and the broad-line region (BLR). The BLR consists of high-velocity gas, which is mainly photoionized by the ultraviolet (UV) and optical photons from the accretion disk. The profile of the broad emission lines traces the kinematic and spatial distribution of the gas (C. M. Urry & P. Padovani 1995). The luminosity variation of the accretion disk will lead to the time-delay responses of the emission-lines (e.g., B. M. Peterson et al. 1992, 2002; K. T. Korista & M. R. Goad 2004; D. Park et al. 2012; A. J. Barth et al. 2015; C. Hu et al. 2015). This time delay can be measured using methods such as the discrete correlation function (DCF; R. A. Edelson & J. H. Krolik 1988), the interpolated cross-correlation function (ICCF; B. M. Peterson et al. 1998), the local cross-correlation function (LCCF; W. F. Welsh 1999), and the running optimal average (ROA) method (F. R. Donnan et al. 2021), among others, to estimate the size of the BLR. Assuming the virial motion of BLR gas, the mass of the SMBH can be estimated from the lag and the full width at half maximum (FWHM) or line dispersion (σ_{line}) of the broad emission lines, with the inclusion of a virial factor f that accounts for the geometry and kinematics of the BLR. This technique is known as reverberation mapping (RM, B. M. Peterson 1993).

However, applying the RM technique to radio-loud AGNs, particularly blazars, remains challenging. For blazars, the jet emission is dominant and highly variable, making it difficult to disentangle variation of the accretion disk from that of jet. Consequently, over the past few decades, RM studies have been successfully carried out for only a limited number of blazars. For the low-synchrotron-peaked source, such as 3C 273, the jet emission is weak in the optical band (S. R. Patel et al. 2021), and the optical emission is dominated by the disk, making RM feasible. The central black hole mass of 3C 273 is estimated to be approximately $4.10 \times 10^8 M_\odot$ (Z.-X. Zhang et al. 2019). On the other hand,

for other sources, the non-thermal dominance (NTD) parameter is employed to classify the data into jet-dominated and disk-dominated states (M. S. Shaw et al. 2012). This method assumes that when $NTD < 2$, the specific fluxes at 5100 Å is dominated by the accretion disk. When performing the lag correlation analysis, data with $NTD > 2$ are excluded. A. Amador-Portes et al. (2024) and A. Amador-Portes et al. (2025) used the NTD method to estimate the central black hole mass of PKS 1510-089 to be $2.85 \times 10^8 M_\odot$. This method relies on a relatively straightforward threshold-based criterion, which may limit its robustness. In other words, even when the NTD is below 2, variability from the jet may still contribute to the observed fluxes, potentially disturbing the correlation analysis. Moreover, for sources where the NTD method cannot be applied, that is, when the majority of data have $NTD > 2$, the only option is to directly measure the time lag between the V -band light curve and the broad emission lines. For example, S. Pandey et al. (2022) measured a time lag of about 70 days between the $H\beta$ line and the V -band light curve in PKS 0736+017, and used this lag to report a central black hole mass of approximately $7.32 \times 10^7 M_\odot$. In their analysis, however, the correlation coefficient of the ICCF was relatively low, with a peak value below 0.5.

In this paper, we present a approach to distinguish the contributions of the accretion disk and the jet, and pave a way for the application of RM for a subclass of blazars. Blazars with broad emission lines are classified as flat-spectrum radio quasars (FSRQs). According to the broad band spectral energy distribution (SED), FSRQs are typically categorized as the low-synchrotron-peaked blazars, with the peak frequency of the synchrotron bump lying below 10^{14} Hz (A. A. Abdo et al. 2010a). Thus, in the optical observation window, the jet emission exhibits a power-law spectrum with negative spectral index in the $\log \nu F_\nu$ versus $\log \nu$ plot. The accretion disk, contributing the big blue bump (BBB) in the SED, usually peaks in the UV band and shows a positive spectral index in the optical window. Therefore, we can predict that the spectroscopic data is expected to show a spectral break when the disk and jet emissions differ by less than a magnitude. Thus, by quantitatively modeling the spectral break, we are able to disentangle the contributions from the accretion disk and the jet. In this work, we select PKS 1510-089 and PKS 0736+017 as case studies to explore the feasibility of this new approach, since both targets have the abundant publicly available spectroscopic data and evident spectral break. The structure of this paper is organized as follows. Section 2 details the data analysis and processing. Section 3 presents the results, and Section 4 offers discussion and conclusions. In addition, the redshift values used in this study are $z = 0.361$ for PKS 1510-089 (E. M. Burbidge & T. D. Kinman 1966) and $z = 0.189$ for PKS 0736+017 (C. R. Lynds 1967).

2. DATA REDUCTION

All spectroscopic data used in this study are from the Steward Observatory⁴. These data were obtained with the 2.3 m Bok Telescope on Kitt Peak and the 1.54 m Kuiper Telescope on Mount Bigelow in Arizona, using the SPOL spectropolarimeter (G. D. Schmidt et al. 1992). A 600 mm^{-1} grating provided a spectral range of 4000-7550 Å with a dispersion of 4 Å /pixel. Depending on the slit width, the spectral resolution was typically 16–24 Å. Flux calibration followed the procedure described in P. S. Smith et al. (2009). The spectra were first calibrated using sensitivity functions derived from spectrophotometric standard stars, and then re-scaled to match the synthetic V -band photometry for each night. The dataset employed in this work has previously been reported in earlier studies (S. Pandey et al. 2022; A. Amador-Portes et al. 2024, 2025). From the public website of the Steward Observatory, we downloaded 371 spectra of PKS 1510-089 (observed between MJD 54,830 and 58,307), 130 spectra of PKS 0736+017 (observed between MJD 56,989 and 58,251). The Galactic interstellar extinction and reddening of all spectra were corrected by the procedure given in J. A. Cardelli et al. (1989), and $E(B-V)$ of sources refers to the NASA/IPAC Extragalactic Database⁵. The spectra spans a frequency range from approximately $10^{14.60}$ to $10^{14.88}$ Hz.

2.1. Spectral Break

The top-left and top-right panels of Figure 1 display spectra of PKS 0736+017 and PKS 1510-089 at three different flux levels. At the low-flux states, the spectra exhibit a concave shape in the plane of $\log \nu$ versus $\log \nu F_\nu$, namely a spectral break. This spectral break shifts, becomes less prominent and gradually disappears at the high-flux levels. The detailed analysis of the spectral break and its dependence on the flux level will be presented in Section 2.4.

To illustrate the origin of the spectral break, we show the low-flux state broadband SEDs of PKS 1510-089 and PKS 0736+017, compiled from historical archival data downloaded from the Space Science Data Center⁶ (SSDC) in bottom

⁴ <https://james.as.arizona.edu/~psmith/Fermi/>

⁵ <https://ned.ipac.caltech.edu/>

⁶ <https://tools.ssdc.asi.it/SED/>

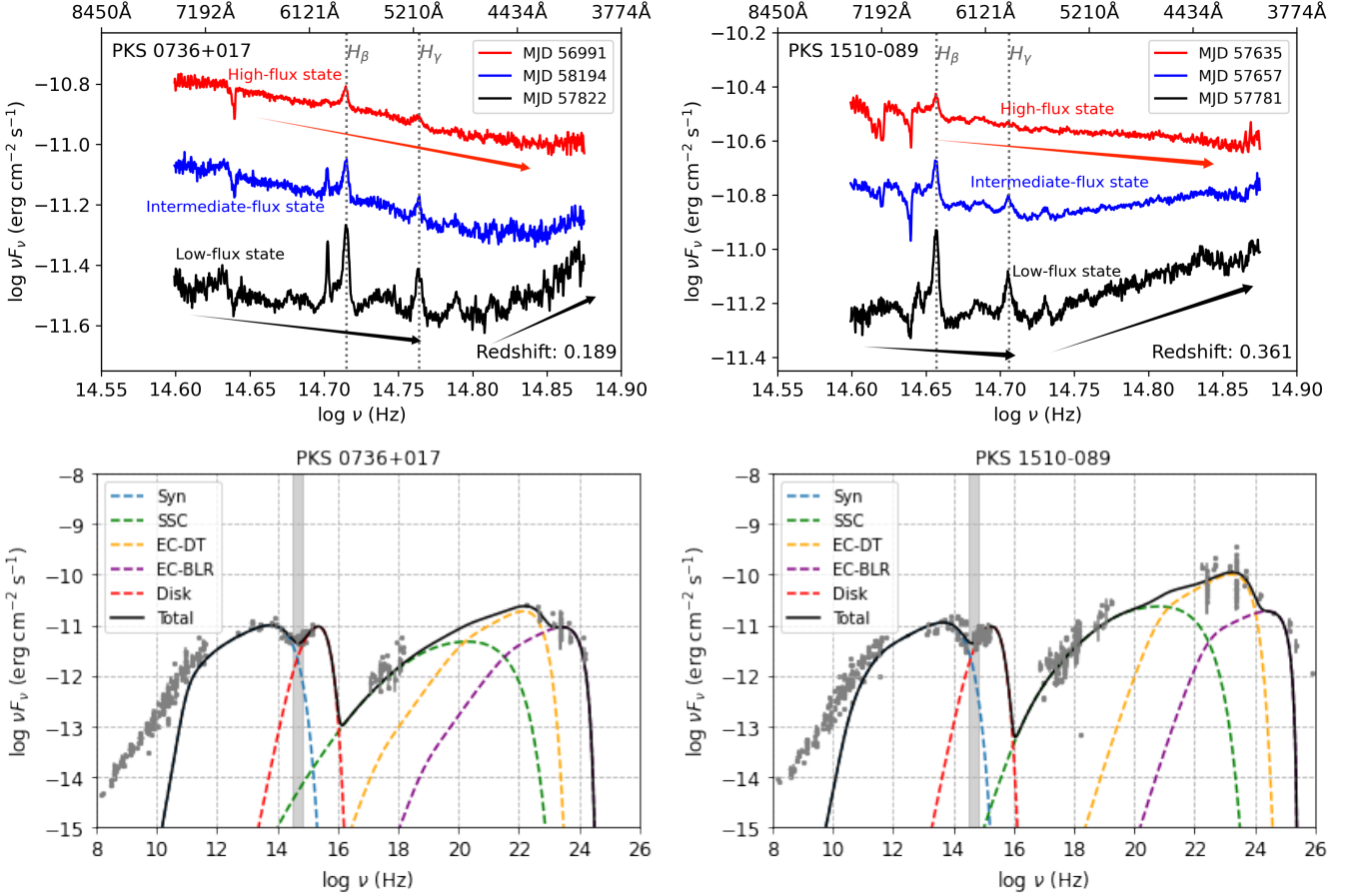


Figure 1. Top panels: Representative optical spectra of PKS 0736+017 (left) and PKS 1510-089 (right) in three different flux states. The arrows approximately mark the local spectral slope, serving as visual guides. Bottom panels: Broadband SEDs in the low-flux state for PKS 0736+017 (left) and PKS 1510-089 (right), compiled from archival data and modeled by using the one-zone leptonic model (see Appendix A). The reduced χ^2 values are 114.03 for PKS 0736+017 and 153.06 for PKS 1510-089, with radio data excluded from the calculation. The shaded gray regions mark the optical observation window. The overlap of jet and disk components confirms that both contribute to the observed optical emission.

panels of Figure 1. We reproduced the broadband SEDs using a one-zone leptonic model. Details of the model and its parameters are provided in Appendix A. Within the observing band, the total energy flux consists of two components, a red component and a blue component. The red component corresponds to the non-thermal synchrotron emission from the jet, while the blue component arises from thermal emission of the accretion disk.

In general, the variability of the jet is more significant than that of the accretion disk. When the target changes from a quiescent state to an active state, both the peak flux and frequency of the jet component increase (C.-Z. Wang & Y.-G. Jiang 2024; J.-T. Wang & Y.-G. Jiang 2025; J. Deng & Y. Jiang 2025). Consequently, the spectral break evident in low-flux states disappears in the high-flux states.

2.2. Emission Lines Fitting Scheme

In this section, we describe the method used to obtain the light curve of emission lines through the spectral fitting procedure. First of all, the observed spectroscopic data were shifted to the rest-frame wavelengths based on their redshifts.

For both targets, the H β and H γ broad lines are present within the optical window, as seen in top panels of Figure 1. In this study, we extracted the light curves of these two lines. Since fitting the entire optical range spectrum with a single power-law function tends to either underestimate the high-frequency end when the low-frequency part is well fitted, or vice versa, we adopted a segmented fitting strategy for each observation ID. Specifically, we divided the spectrum into four wavelength regions: (i) 4435–4685 Å, dominated by Fe II features, used to determine the parameters

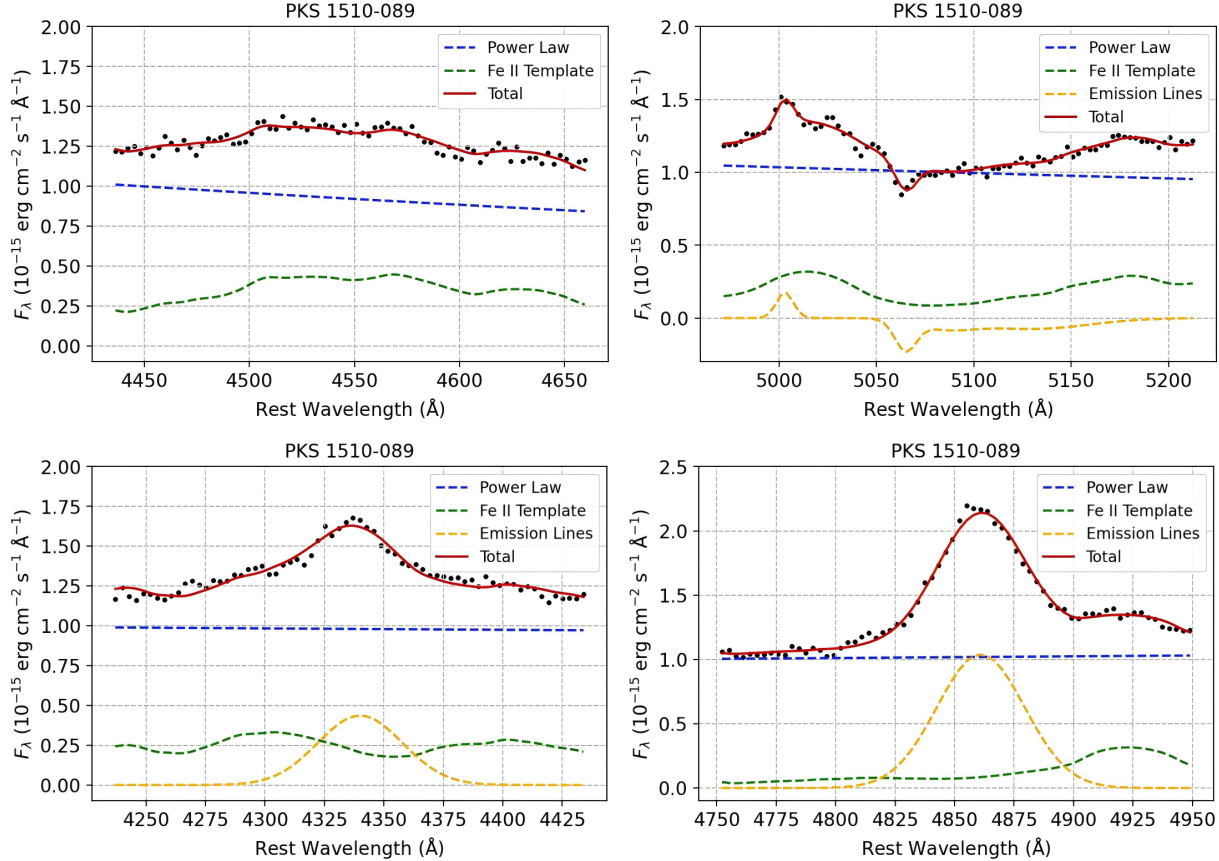


Figure 2. An example of the spectral decomposition for PKS 1510–089, using the spectrum observed on MJD 58253.

of the Fe II emission lines with the template taken from [T. A. Boroson & R. F. Green \(1992\)](#); (ii) 4200–4435 Å, with the Fe II template parameters from step (i), to measure the H γ flux; (iii) 4750–4950 Å, to measure the H β flux; and (iv) 4980–5230 Å, used to determine the 5100 Å continuum flux, also including the Fe II contribution fixed from (i). The [O III] line was fixed during the fitting, with its parameters obtained from the average spectrum. For PKS 1510–089, a prominent telluric absorption feature is present near 5100 Å. We corrected for this feature following the same procedure as [A. Amador-Portes et al. \(2024\)](#), by modeling it with three Gaussian components. The fitting was performed in Python, employing the minimize function from SciPy ([P. Virtanen et al. 2020](#)) to obtain the best-fit parameters. Figure 2 illustrates an example of the spectral decomposition for PKS 1510–089, using the spectrum observed on MJD 58253. Through the numerical integration of the Gaussian functions, we obtained the flux of the emission lines. The light curves of the emission lines and 5100 Å continuum are shown in Figure 4.

2.3. Disentangle the disk and jet

To disentangle the emission from the accretion disk and the jet, we employed a broader spectral range ($\log \nu$ [Hz] from 14.60 to 14.88) rather than the narrow range used in Section 2.2. The jet component was modeled with a power-law spectrum with a negative spectral index, while the accretion disk was modeled by the Shakura-Sunyaev model ([N. I. Shakura & R. A. Sunyaev 1973](#)). All disk parameters except the luminosity were fixed based on the fitting result of the broad band SEDs shown in bottom panels of Figure 1.

We first subtracted the contributions of the Fe II emission with parameters adopted from the fit in Section 2.2. Second, we excluded the spectral ranges containing prominent emission lines and atmospheric absorption. Specifically, we masked the 4800–4900 Å around H β λ 4861, the 4950–5050 Å around [O III] λ 5007, and the 4300–4400 Å around H γ λ 4340. The spectra at different epochs may have different ratio of jet over disk components. In particular, during high-flux states, as shown in the top panels of Figure 1, the disk contribution becomes negligible due to the disappearance of the spectral break, and including a disk component in the fit does not yield reliable results. Thus, we consider

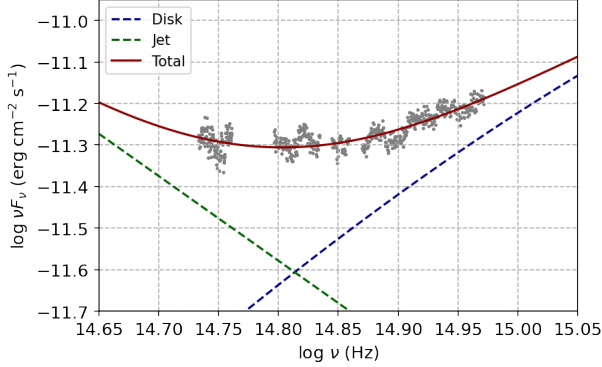


Figure 3. Spectral decomposition of PKS 1510-089 on MJD 58253, shown as a representative example to illustrate the disk-jet emission separation method. The gray points show the optical spectrum after removal of the Fe II emission, prominent emission lines, and atmospheric absorption features. The green dashed line represents the power-law component corresponding to non-thermal jet emission, while the blue dashed line represents thermal emission from the accretion disk, modeled with the Shakura-Sunyaev model. The red solid line shows the total emission combining both components. The reduced χ^2 value of the fit is 0.28.

three fitting models, i.e., (1) only the jet, (2) only the disk, and (3) both the jet and the disk. For each case, we calculated the value of Akaike Information Criterion (AIC), which considers the trade-off between goodness of fit and model complexity. The lower value of AIC indicates a better result. In many cases, the case (3) gives the lowest AIC, suggesting that the jet and disk have comparable contributions, as shown in Figure 3. At high flux states, case (1) gives the lowest AIC, which indicates the dominance of jet component. However, across all observed spectra of PKS 1510-089 and PKS 0736+017, we did not find any epoch in which the case (2) yielded the lowest AIC. In addition, the jet-only model (case 1) provides the lowest AIC in 28% of the observations for PKS 1510-089, and in 22% of the observations for PKS 0736+017. Figure 3 presents an example of the fit by case 2. Finally, the fluxes of the disk and jet components within the observed frequency range were calculated via numerical integration. The light curves of the disk and jet component for the two targets are plotted in Figure 4.

2.4. NTD parameters

In this section, we calculated the NTD parameter using both the conventional method and the results of the decomposition described in Section 2.3, and compared them. Specifically, according to the conventional definition, $\text{NTD} = L_{\text{obs}}^{5100}/L_{\text{disk}}^{5100}$, where L_{obs}^{5100} is the observed continuum luminosity at 5100 Å, and L_{disk}^{5100} represents the disk luminosity at 5100 Å predicted from the H β emission using the empirical relation provided by [S. Rakshit et al. \(2020\)](#):

$$\log L_{\text{H}\beta} = (1.057 \pm 0.002) \log L_{\text{disk}}^{5100} + (-4.41 \pm 0.10). \quad (1)$$

The variations of the NTD parameter are presented in the top panel of Figure 4, where the gray dashed line marks $\text{NTD}=2$. On the other hand, as described in Section 2.3, we decomposed the disk and jet components by fitting the spectral break. This method was successfully applied to most observation IDs for the two blazars. Accordingly, we also calculated the NTD parameters based on the disk flux obtained from the spectral break fitting. To distinguish them from the conventional estimates, we denote the parameters derived from this method as NTD^* , which is given by

$$\text{NTD}^* = (L_{\text{jet}}^{5100} + L_{\text{disk}}^{5100})/L_{\text{disk}}^{5100}. \quad (2)$$

The bottom panel in Figure 4 shows the results, and the dashed line also marks $\text{NTD}^*=2$. By comparing the two panels, it can be seen that for both blazars, very few observation IDs have $\text{NTD}^* < 2$, whereas nearly half of the observations yield $\text{NTD}^* > 2$. This indicates that the disk flux estimated from Equation (1) may be overestimated in blazars. In addition, Figure 5 shows the variation of the spectral break frequency ν_{SB} with NTD^* for the two blazars. It can be seen that when $\text{NTD}^* \gtrsim 6$ for PKS 1510-089 and $\text{NTD}^* \gtrsim 5$ for PKS 0736+017, the spectral break is difficult to be observed within the optical window.

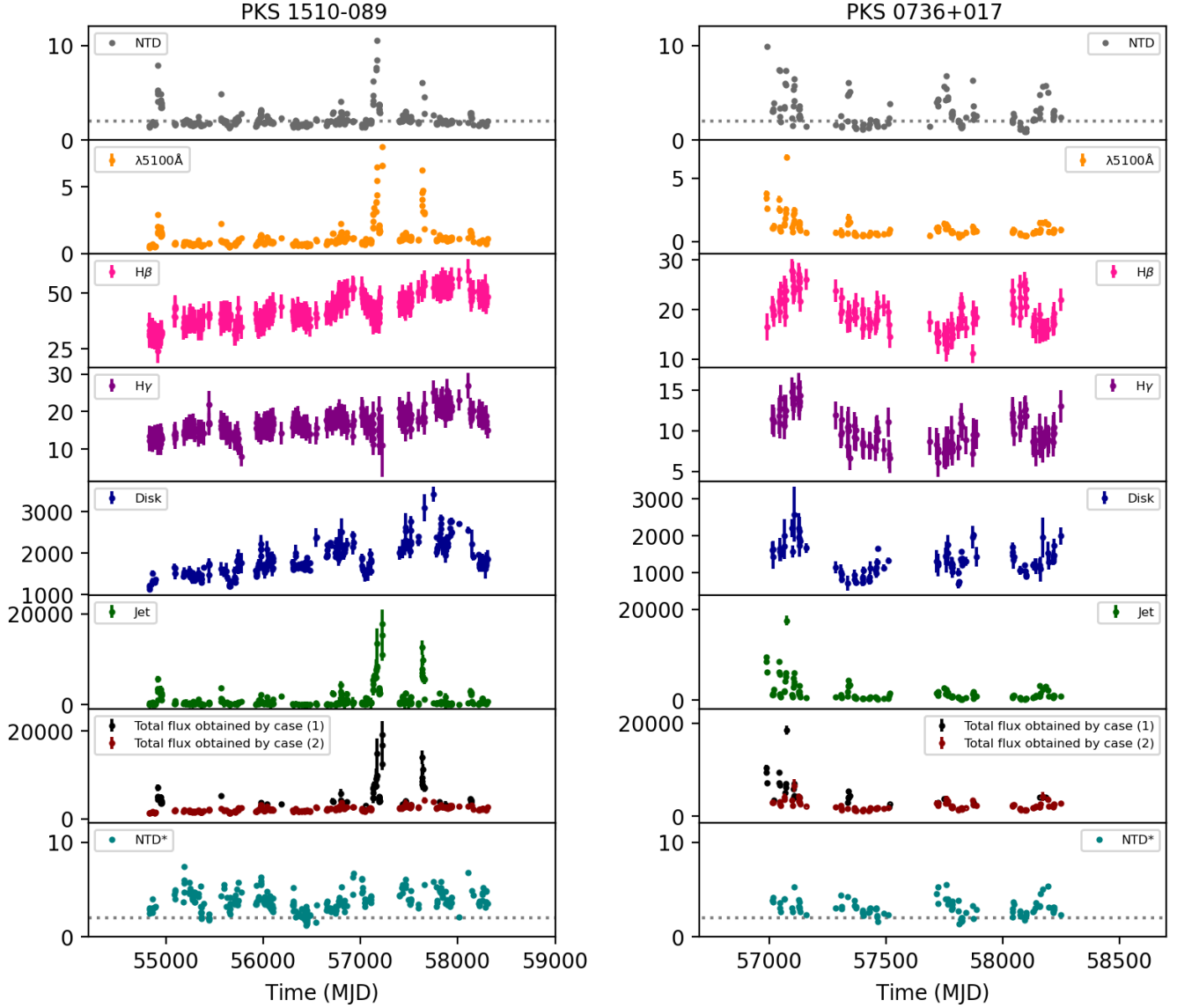


Figure 4. From top to bottom: light curves of the NTD parameter, $\lambda 5100\text{\AA}$ continuum, broad emission lines ($H\beta$ and $H\gamma$), jet, accretion disk, total flux (disk+jet), and the NTD^* parameter for PKS 0736+017 (right) and PKS 1510-089 (left). Grey dashed lines in the top (NTD) and bottom (NTD^*) panels indicate $NTD=2$ and $NTD^*=2$, respectively. The Y-axis units are as follows: NTD and NTD^* are dimensionless, the $\lambda 5100\text{\AA}$ continuum is in $10^{-15}\text{ erg cm}^{-2}\text{ s}^{-1}\text{ \AA}^{-1}$, all other panels are in $10^{-15}\text{ erg cm}^{-2}\text{ s}^{-1}$.

3. REVERBERATION MAPPING

In this work, we first employed the ICCF method (B. M. Peterson et al. 1998) for the correlation analysis, following the procedure described in S. Pandey et al. (2022). Figure A1 shows the correlation between the disk and $H\beta$, as well as the correlation between the disk and $H\gamma$ for PKS 1510-089. Figure A2 presents the corresponding results for PKS 0736+017. In both sources, the variations of $H\beta$ and $H\gamma$ are found to lag behind those of the disk. Second, we applied the ROA method (F. R. Donnan et al. 2021) for comparison. Figures A3 and A4 show the ROA results for PKS 1510-089 and PKS 0736+017, respectively. The derived time lags for the both methods are summarized in Table 1. The results from the ICCF and ROA methods are consistent within uncertainties, with ROA providing slightly smaller errors.

To estimate the black hole masses, we measured the FWHM and line dispersion (σ_{line}) of the emission lines from both the mean and root-mean-square (RMS) spectra, following the procedure described in B. M. Peterson et al. (2004).

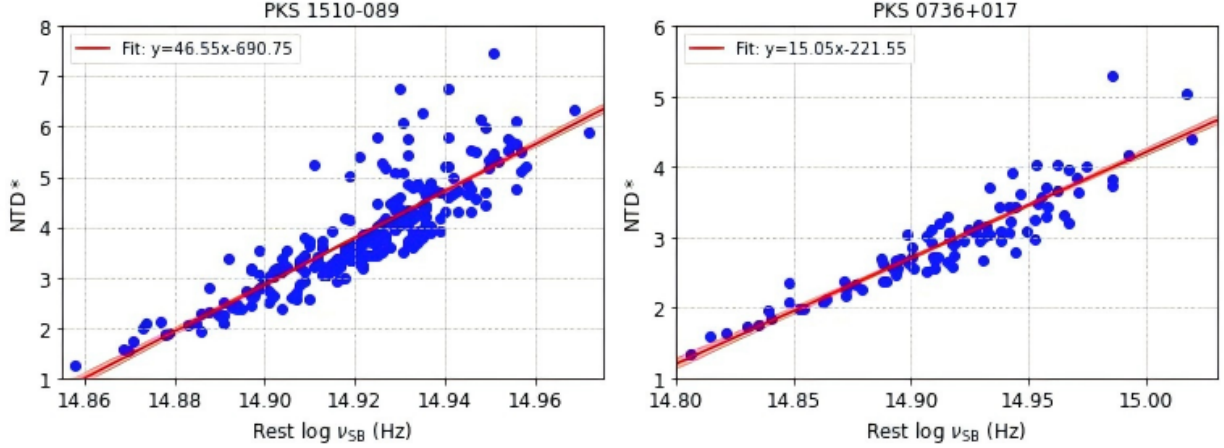


Figure 5. Relationship between the rest frequency of spectral break and the value of NTD*. The left panel shows PKS 1510-089, and the right panel shows PKS 0736+017. The red lines indicate the results of linear fits.

Table 1. Results of lag measurements (in days) for PKS 1510-089 and PKS 0736+017.

	PKS 1510-089		PKS 0736+017	
	Disk vs H β	Disk vs H γ	Disk vs H β	Disk vs H γ
ROA	$-110.9^{+16.2}_{-16.0}$	$-94.1^{+13.5}_{-12.9}$	$-67.1^{+11.6}_{-11.9}$	$-65.8^{+21.1}_{-19.0}$
ICCF	$-134.3^{+36.2}_{-37.0}$	$-91.3^{+37.4}_{-43.1}$	$-53.2^{+23.3}_{-29.4}$	$-59.9^{+21.5}_{-17.5}$

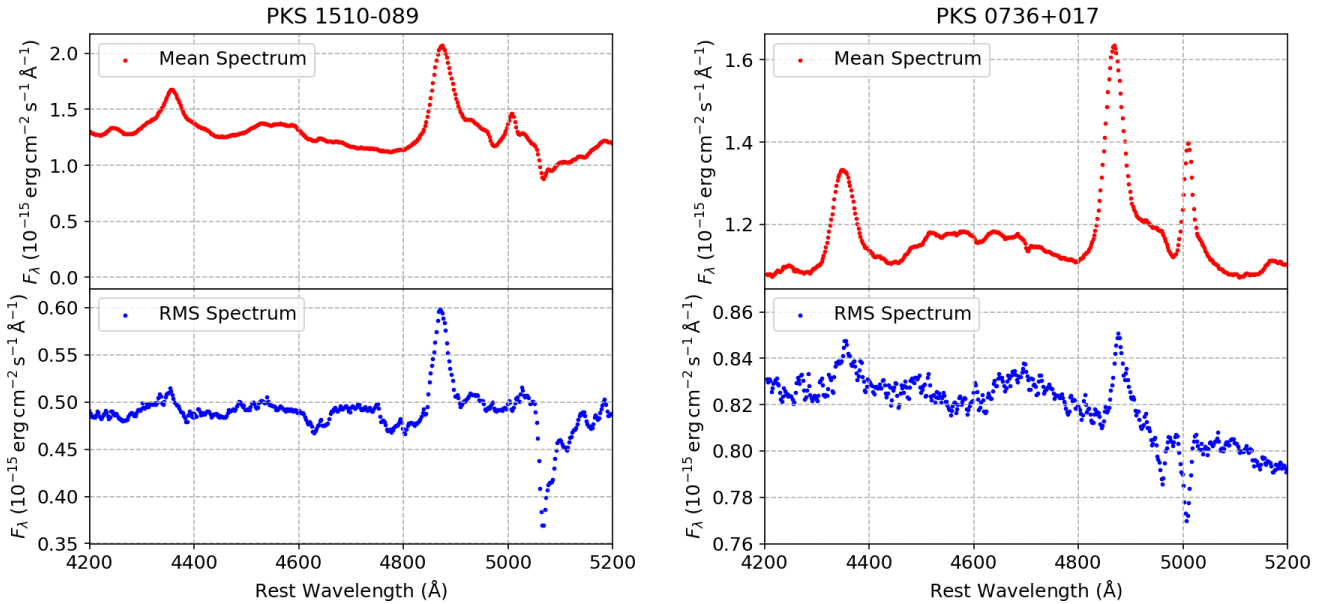


Figure 6. Mean (top panels, red dots) and RMS (bottom panels, blue dots) spectra for the blazars PKS 1510-089 (left) and PKS 0736+017 (right).

The mean and RMS spectra for the two blazars are shown in Figure 6. As evident in the RMS spectra, the H γ line is very weak, rendering its measurements unreliable. Therefore, in the RMS spectra, we only measured the FWHM and σ_{line} for H β . In the mean spectra, we measured the FWHM and σ_{line} for both H γ and H β . The measured values of both FWHM and σ_{line} for the two blazars are summarized in Table 2.

Table 2. Measurements of emission line widths and black hole masses obtained from the mean and rms spectra.

		PKS 1510-089			PKS 0736+017		
		Type	ΔV (km s $^{-1}$)	M_{BH} ($10^7 M_{\odot}$)	Type	ΔV (km s $^{-1}$)	M_{BH} ($10^7 M_{\odot}$)
Mean	H β	FWHM	2295 ± 243	$12.6_{-3.0}^{+3.6}$	FWHM	1938 ± 278	$5.5_{-1.6}^{+2.1}$
		σ_{line}	1250 ± 120	$14.9_{-3.3}^{+3.9}$		1139 ± 121	$7.5_{-1.9}^{+2.3}$
	H γ	FWHM	2335 ± 260	$11.1_{-2.7}^{+3.2}$	FWHM	2731 ± 254	$10.5_{-3.6}^{+4.2}$
		σ_{line}	1446 ± 132	$17.0_{-3.7}^{+4.3}$		1379 ± 139	$10.7_{-3.6}^{+4.4}$
RMS	H β	FWHM	2073 ± 121	$10.4_{-1.8}^{+2.0}$	FWHM	2054 ± 189	$6.2_{-1.3}^{+1.5}$
		σ_{line}	1298 ± 132	$16.1_{-3.7}^{+4.5}$		1207 ± 138	$8.4_{-2.3}^{+2.7}$
	H γ	FWHM	-	-	FWHM	-	-
		σ_{line}	-	-		σ_{line}	-

Using the measured time lags together with the FWHM or σ_{line} values, we estimated the black hole masses of both blazars. The black hole mass is calculated using the formula from B. M. Peterson et al. (2004):

$$M_{\text{BH}} = f \frac{R_{\text{BLR}} \Delta V^2}{G} = f \frac{c\tau \Delta V^2}{G}, \quad (3)$$

where f is set to be 1.12 for FWHM and 4.47 for σ_{line} (J.-H. Woo et al. 2015); c is the speed of light; $R_{\text{BLR}} = c\tau$ is the BLR size; G is the gravitational constant; and ΔV represents the velocity width of the broad line. Since the time lag measured with ROA provides a smaller uncertainty, we adopted the τ values of ROA for the black hole mass calculation. The measured black hole masses based on different emission lines and using both FWHM and σ_{line} values are summarized in Table 2. For PKS 1510-089, the derived average black hole mass is $1.4 \times 10^8 M_{\odot}$, while for PKS 0736+017, the average mass is $8.1 \times 10^7 M_{\odot}$. Following S. Kaspi et al. (2000) and T. Beckert & W. J. Duschl (2002), we estimated the mass accretion rates normalized by the Eddington accretion rate (\dot{m}) for both sources, using the black hole masses and the average disk luminosities at 5100 Å. The resulting normalized accretion rate is $\dot{m} \approx 0.26$ for PKS 1510-089 and $\dot{m} \approx 0.14$ for PKS 0736+017.

4. DISCUSSION AND CONCLUSION

Previous studies have made efforts to perform reverberation mapping on the blazars PKS 1510-089 and PKS 0736+017, both of which relied on the NTD parameter to separate disk and jet contributions. For PKS 1510-089, A. Amador-Portes et al. (2024) performed a correlation analysis between the H β line and the 5100 Å continuum after excluding data points with $\text{NTD} > 2$, and reported a time lag of about 80 days. This approach is feasible primarily because that the accretion disk in PKS 1510-089 is intrinsically bright, with only about 39% of the data points showing $\text{NTD} > 2$. In contrast, for PKS 0736+017, S. Pandey et al. (2022) also calculated the NTD values and found that the average NTD is as high as 2.7. This indicates that the majority of the 5100 Å data points are jet-dominated. If all data points with $\text{NTD} > 2$ are excluded, more than half (about 67%) of the dataset would be removed, making it difficult to conduct a reliable correlation analysis. In our algorithm, the filtered data points with valid disk fluxes are 72% of all measurements for PKS 0736+017. Thus, our algorithm excludes only 28% of the data, significantly fewer than the 67% of the data under the NTD-based selection.

Previous studies have reported a wide range of black hole mass estimation for these two blazars based by other methods. For PKS 1510-089, by modeling the temperature profile of the accretion disk, A. A. Abdo et al. (2010b) and G. Castignani et al. (2017) inferred the black hole mass to be $5.4 \times 10^8 M_{\odot}$ and $2.4 \times 10^8 M_{\odot}$, respectively. In addition, using the single-epoch spectrum method, A. Y. K. N. Oshlack et al. (2002) and G. Z. Xie et al. (2005) derived masses of $3.9 \times 10^8 M_{\odot}$ and $2.0 \times 10^8 M_{\odot}$ from the $\lambda 5100$ continuum luminosity and the FWHM of the H β line. In comparison, the black hole mass of PKS 1510-089 from our RM ($1.4 \times 10^8 M_{\odot}$) is relatively smaller than those derived by other methods. For PKS 0736+017, R. J. McLure & J. S. Dunlop (2001) and J.-H. Woo & C. M. Urry (2002) presented a black hole mass of $2.9 \times 10^8 M_{\odot}$ and $1.0 \times 10^8 M_{\odot}$ by using bolometric luminosity. Our RM measurement yields $8.1 \times 10^7 M_{\odot}$, which is also relatively smaller. This discrepancy may be due to an overestimation of the disk luminosity in blazars by those methods.

In summary, we proposed a novel approach to perform the reverberation mapping method for blazars by disentangling the disk and jet components through modeling the spectral break in the $\log \nu$ versus $\log \nu F_{\nu}$ plane. Applying this

method to PKS 1510-089 and PKS 0736+017, we obtained the light curves of the accretion disk and emission lines, and obtained the fiducial lags between them. In PKS 1510-089, the $H\gamma$ variability lags behind the accretion disk by approximately 94 days, while the $H\beta$ line shows a lag of about 111 days relative to the disk. In PKS 0736+017, the $H\gamma$ variability lags behind the disk by roughly 66 days, and the $H\beta$ line exhibits a lag of about 67 days. Based on these measured time lags, we estimate black hole masses of $\sim 1.4 \times 10^8 M_\odot$ for PKS 1510-089 and $\sim 8.1 \times 10^7 M_\odot$ for PKS 0736+017, respectively. Compared to traditional NTD-based selection methods, our approach retains more data and provides more significant lag estimation. Thus, our method paves a way to measure the black hole mass for specific jet-dominated AGNs.

ACKNOWLEDGMENTS

The data underlying this article were accessed from the Steward Observatory data base with the following link: <http://james.as.arizona.edu/~psmith/Fermi/> (see, [P. S. Smith et al. 2009](#)). This work has been funded by the National Natural Science Foundation of China under grant No. U2031102, and the Shandong Provincial Natural Science Foundation under grant No. ZR2023MA036.

Software: agnpy ([C. Nigro et al. 2022](#)), SciPy ([P. Virtanen et al. 2020](#)), PyROA ([F. R. Donnan et al. 2021](#))

APPENDIX

A. MULTI-WAVELENGTH SED MODEL

We employed the traditional one-zone leptonic model to reproduce the broadband SEDs presented in bottom panels of Figure 1. This model, widely used for blazars, assumes a homogeneous spherical emission region of radius R , embedded in a magnetic field B . The region moves relativistically along the jet with a velocity $v = \beta c$, corresponding to a bulk Lorentz factor $\Gamma = (1 - \beta^2)^{-1/2}$. A Doppler factor $\delta = [\Gamma(1 - \beta \cos \theta)]^{-1} \approx \Gamma$ is adopted, assuming a small viewing angle $\theta < 1/\Gamma$, typical for blazar jets. The radiative processes include the synchrotron emission, the synchrotron self-Compton (SSC), and external Compton (EC) process. The calculation of spectrum refers to [G. B. Rybicki & A. P. Lightman \(1979\)](#).

Following [S.-J. Kang et al. \(2016\)](#); [R. Khatoon et al. \(2022\)](#); [J. Deng & Y. Jiang \(2023\)](#), we assumed that the electron energy distribution in the emission zone follows a broken power-law, characterized by spectral indices p_1 and p_2 below and above the broken Lorentz factor γ_b , respectively. The distribution is expressed as:

$$N(\gamma) = \begin{cases} N_0 \gamma^{-p_1} & \gamma_{\min} \leq \gamma \leq \gamma_b, \\ N_0 \gamma_b^{p_2 - p_1} \gamma^{-p_2} & \gamma_b < \gamma \leq \gamma_{\max} \end{cases} \quad (\text{A1})$$

where γ_{\min} and γ_{\max} are the minimal and maximal electron Lorentz factors, and N_0 is the normalized particle number density.

For the EC emission, the seed photons are assumed to originate from both the BLR and the DT. Following [R. Khatoon et al. \(2022\)](#); [J. Deng & Y. Jiang \(2024\)](#), we model the photon fields from the BLR and DT as single-temperature blackbody spectra with temperatures of $T_{\text{BLR}} = 4.2 \times 10^4$ K and $T_{\text{DT}} = 10^3$ K, respectively. Their photon energy densities, u_{BLR} and u_{DT} , are treated as free parameters.

We model the accretion disk as a geometrically thin, optically thick Shakura–Sunyaev disk ([N. I. Shakura & R. A. Sunyaev 1973](#)), using the agnpy⁷ Python package ([C. Nigro et al. 2022](#)). The inner and outer disk radii are set to the default values, $R_{\text{in}} = 6 R_g$ and $R_{\text{out}} = 200 R_g$, where R_g is the gravitational radius. The radiative efficiency is also fixed $\eta = 1/12$, representing the fraction of accreted mass energy converted into radiation. As a result, the accretion disk component only has two free parameters: the black hole mass (M_{BH}) and the disk luminosity (L_{disk}).

To reproduce the broadband SED, a total of thirteen parameters are required: N_0 , γ_{\min} , γ_b , γ_{\max} , p_1 , p_2 , B , R , δ , u_{DT} , u_{BLR} , L_{disk} , and M_{BH} . Given the complexity of the parameter space, applying rigorous optimization methods

⁷ <https://agnpy.readthedocs.io/en/latest/index.html>

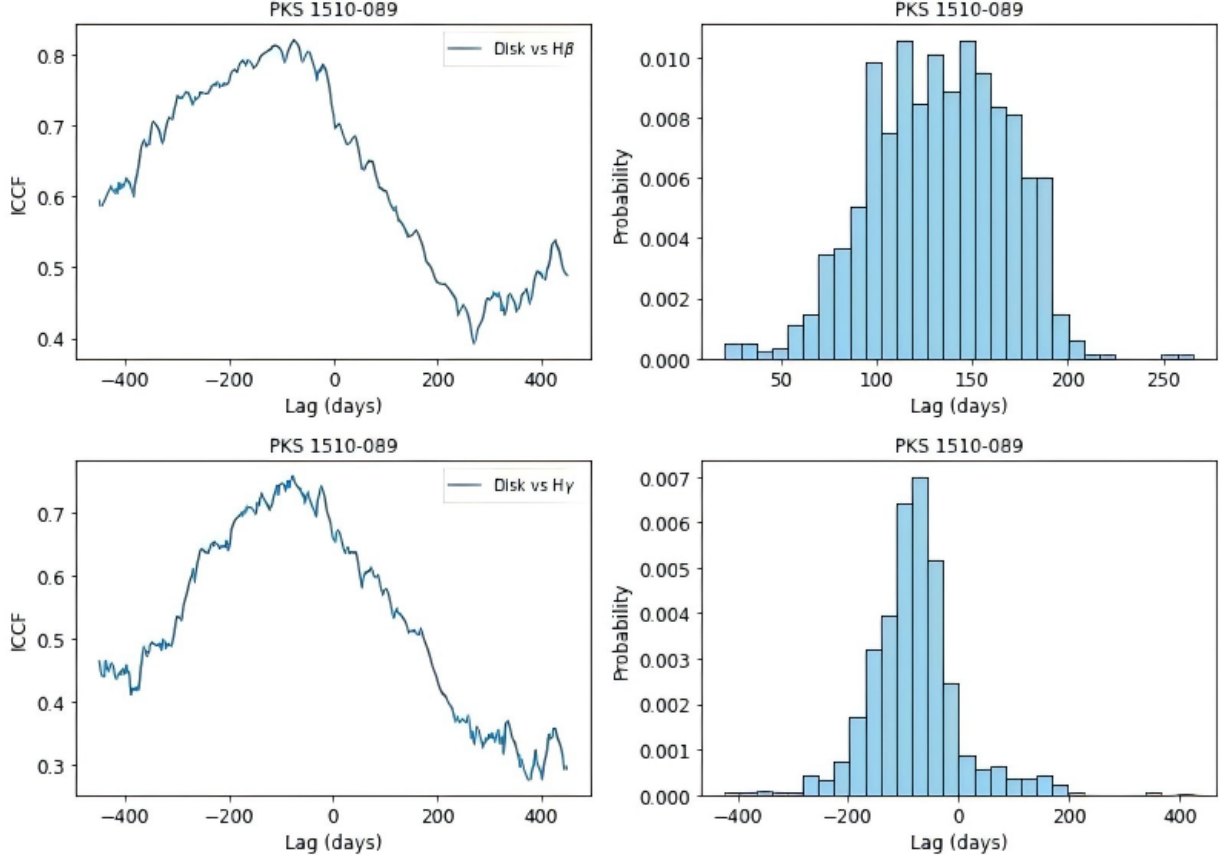


Figure A1. Top panels: ICCF (left) and centroid probability distribution (right) between the disk continuum and the $H\beta$ line in PKS 1510-089. Bottom panels: Same as above, but for the $H\gamma$ line.

such as MCMC would be computationally expensive and difficult to converge. Thus, the model parameters were tested within feasible values to fit the SEDs by eye estimation such as A. Roy et al. (2021). Finally, for PKS 1510-089, the adopted model parameters are as follows: $N_0 = 398 \text{ cm}^{-3}$, $\gamma_{\min} = 300$, $\gamma_b = 500$, $\gamma_{\max} = 10000$, $p_1 = 1.3$, $p_2 = 2.3$, $B = 0.016 \text{ G}$, $R = 0.01 \text{ pc}$, $\delta = 32$, $u_{\text{DT}} = 9 \times 10^{-5} \text{ erg cm}^{-3}$, $u_{\text{BLR}} = 3 \times 10^{-5} \text{ erg cm}^{-3}$, $L_{\text{disk}} = 4 \times 10^{45} \text{ erg s}^{-1}$, $M_{\text{BH}} = 3 \times 10^8 M_{\odot}$. For PKS 0736+017, the adopted model parameters are as follows: $N_0 = 251 \text{ cm}^{-3}$, $\gamma_{\min} = 10$, $\gamma_b = 300$, $\gamma_{\max} = 4600$, $p_1 = 1.3$, $p_2 = 2.3$, $B = 0.25 \text{ G}$, $R = 0.01 \text{ pc}$, $\delta = 11$, $u_{\text{DT}} = 4 \times 10^{-3} \text{ erg cm}^{-3}$, $u_{\text{BLR}} = 3 \times 10^{-3} \text{ erg cm}^{-3}$, $L_{\text{disk}} = 4 \times 10^{45} \text{ erg s}^{-1}$, $M_{\text{BH}} = 2 \times 10^8 M_{\odot}$.

B. PLOTS OF ICCF AND ROA FOR PKS 1510-089 AND PKS 0736+017

REFERENCES

Abdo, A. A., Ackermann, M., Ajello, M., et al. 2010a, ApJ, 715, 429, doi: [10.1088/0004-637X/715/1/429](https://doi.org/10.1088/0004-637X/715/1/429)

Abdo, A. A., Ackermann, M., Agudo, I., et al. 2010b, ApJ, 721, 1425, doi: [10.1088/0004-637X/721/2/1425](https://doi.org/10.1088/0004-637X/721/2/1425)

Amador-Portes, A., Chavushyan, V., Patiño-Álvarez, V. M., & Ramón-Valdés, J. 2025, ApJ, 979, 227, doi: [10.3847/1538-4357/ada38b](https://doi.org/10.3847/1538-4357/ada38b)

Amador-Portes, A., García-Pérez, A., Chavushyan, V., & Patiño-Álvarez, V. M. 2024, ApJ, 977, 178, doi: [10.3847/1538-4357/ad8ddd](https://doi.org/10.3847/1538-4357/ad8ddd)

Barth, A. J., Bennert, V. N., Canalizo, G., et al. 2015, ApJS, 217, 26, doi: [10.1088/0067-0049/217/2/26](https://doi.org/10.1088/0067-0049/217/2/26)

Beckert, T., & Duschl, W. J. 2002, A&A, 387, 422, doi: [10.1051/0004-6361:20020438](https://doi.org/10.1051/0004-6361:20020438)

Boroson, T. A., & Green, R. F. 1992, ApJS, 80, 109, doi: [10.1086/191661](https://doi.org/10.1086/191661)

Burbidge, E. M., & Kinman, T. D. 1966, ApJ, 145, 654, doi: [10.1086/148808](https://doi.org/10.1086/148808)

Cardelli, J. A., Clayton, G. C., & Mathis, J. S. 1989, ApJ, 345, 245, doi: [10.1086/167900](https://doi.org/10.1086/167900)

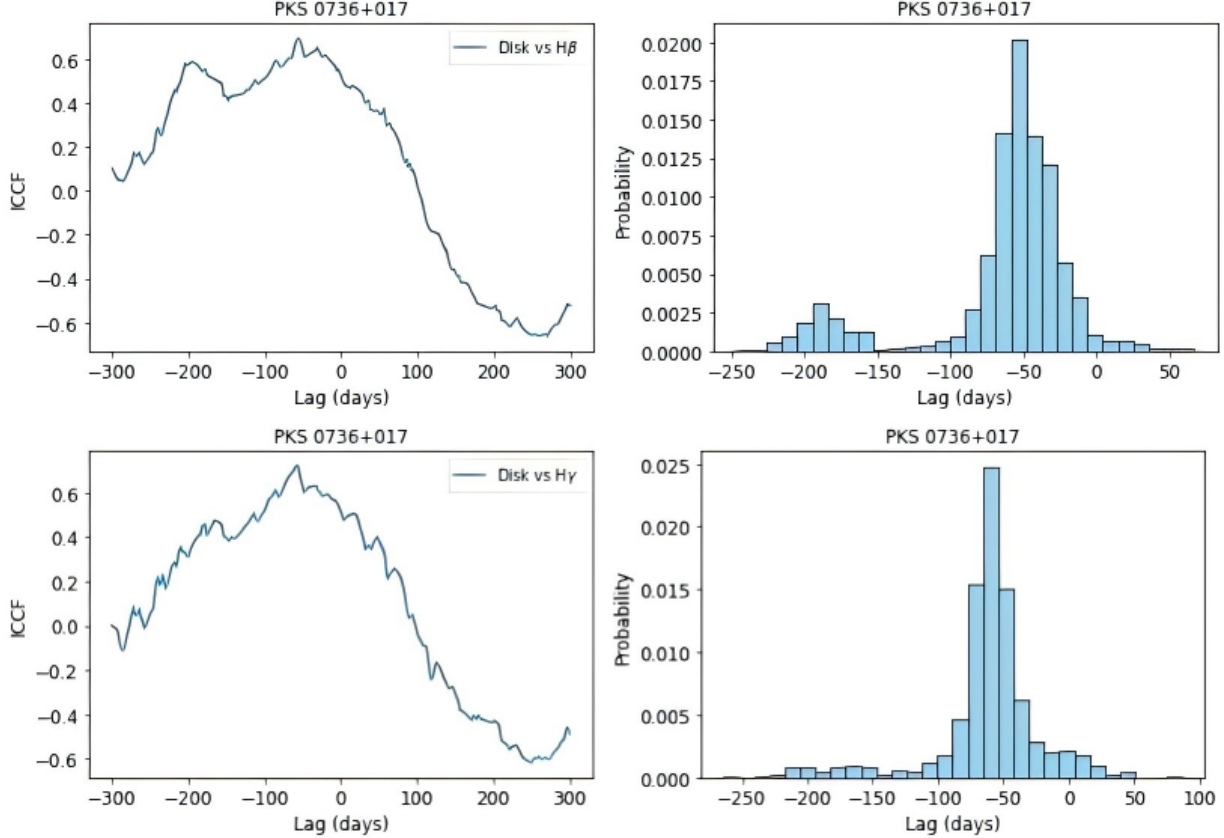


Figure A2. Top panels: ICCF (left) and centroid probability distribution (right) between the disk continuum and the H β line in PKS 0736+017. Bottom panels: Same as above, but for the H γ line.

Castignani, G., Pian, E., Belloni, T. M., et al. 2017, A&A, 601, A30, doi: [10.1051/0004-6361/201629775](https://doi.org/10.1051/0004-6361/201629775)

Deng, J., & Jiang, Y. 2023, MNRAS, 521, 6210, doi: [10.1093/mnras/stad821](https://doi.org/10.1093/mnras/stad821)

Deng, J., & Jiang, Y. 2024, PASP, 136, 124101, doi: [10.1088/1538-3873/ad95bc](https://doi.org/10.1088/1538-3873/ad95bc)

Deng, J., & Jiang, Y. 2025, ApJ, 983, 128, doi: [10.3847/1538-4357/adc106](https://doi.org/10.3847/1538-4357/adc106)

Donnan, F. R., Horne, K., & Hernández Santisteban, J. V. 2021, MNRAS, 508, 5449, doi: [10.1093/mnras/stab2832](https://doi.org/10.1093/mnras/stab2832)

Edelson, R. A., & Krolik, J. H. 1988, ApJ, 333, 646, doi: [10.1086/166773](https://doi.org/10.1086/166773)

Hu, C., Du, P., Lu, K.-X., et al. 2015, ApJ, 804, 138, doi: [10.1088/0004-637X/804/2/138](https://doi.org/10.1088/0004-637X/804/2/138)

Kang, S.-J., Zheng, Y.-G., Wu, Q., & Chen, L. 2016, MNRAS, 461, 1862, doi: [10.1093/mnras/stw1312](https://doi.org/10.1093/mnras/stw1312)

Kaspi, S., Smith, P. S., Netzer, H., et al. 2000, ApJ, 533, 631, doi: [10.1086/308704](https://doi.org/10.1086/308704)

Khatoon, R., Prince, R., Shah, Z., Sahayanathan, S., & Gogoi, R. 2022, MNRAS, 513, 611, doi: [10.1093/mnras/stac892](https://doi.org/10.1093/mnras/stac892)

Korista, K. T., & Goad, M. R. 2004, ApJ, 606, 749, doi: [10.1086/383193](https://doi.org/10.1086/383193)

Lynds, C. R. 1967, ApJ, 147, 837, doi: [10.1086/149068](https://doi.org/10.1086/149068)

McLure, R. J., & Dunlop, J. S. 2001, MNRAS, 327, 199, doi: [10.1046/j.1365-8711.2001.04709.x](https://doi.org/10.1046/j.1365-8711.2001.04709.x)

Nigro, C., Sitarek, J., Gliwny, P., et al. 2022, A&A, 660, A18, doi: [10.1051/0004-6361/202142000](https://doi.org/10.1051/0004-6361/202142000)

Oshlack, A. Y. K. N., Webster, R. L., & Whiting, M. T. 2002, ApJ, 576, 81, doi: [10.1086/341729](https://doi.org/10.1086/341729)

Pandey, S., Rakshit, S., Woo, J.-H., & Stalin, C. S. 2022, MNRAS, 516, 2671, doi: [10.1093/mnras/stac2418](https://doi.org/10.1093/mnras/stac2418)

Park, D., Woo, J.-H., Treu, T., et al. 2012, ApJ, 747, 30, doi: [10.1088/0004-637X/747/1/30](https://doi.org/10.1088/0004-637X/747/1/30)

Patel, S. R., Bose, D., Gupta, N., & Zuberi, M. 2021, Journal of High Energy Astrophysics, 29, 31, doi: [10.1016/j.jheap.2020.12.001](https://doi.org/10.1016/j.jheap.2020.12.001)

Peterson, B. M. 1993, PASP, 105, 247, doi: [10.1086/133140](https://doi.org/10.1086/133140)

Peterson, B. M., Wanders, I., Bertram, R., et al. 1998, ApJ, 501, 82, doi: [10.1086/305813](https://doi.org/10.1086/305813)

Peterson, B. M., Alloin, D., Axon, D., et al. 1992, ApJ, 392, 470, doi: [10.1086/171447](https://doi.org/10.1086/171447)

Peterson, B. M., Berlind, P., Bertram, R., et al. 2002, ApJ, 581, 197, doi: [10.1086/344197](https://doi.org/10.1086/344197)

Peterson, B. M., Ferrarese, L., Gilbert, K. M., et al. 2004, ApJ, 613, 682, doi: [10.1086/423269](https://doi.org/10.1086/423269)

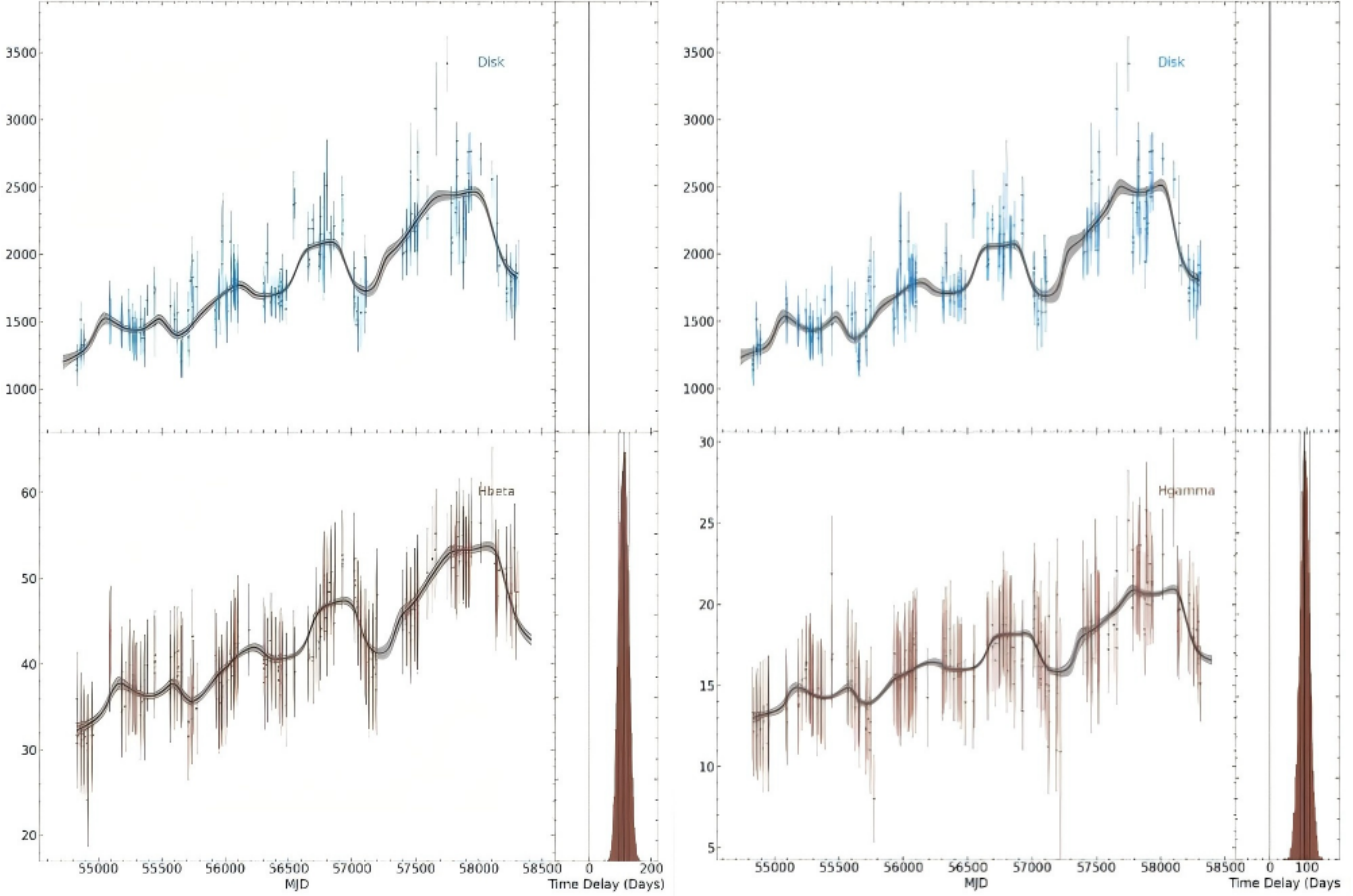


Figure A3. The figure shows the PyROA output for PKS 1510-089. The left panel displays the result between the disk and the $H\beta$ line, while the right panel shows the result with the $H\gamma$ line.

Rakshit, S., Stalin, C. S., & Kotilainen, J. 2020, ApJS, 249, 17, doi: [10.3847/1538-4365/ab99c5](https://doi.org/10.3847/1538-4365/ab99c5)

Roy, A., Patel, S. R., Sarkar, A., Chatterjee, A., & Chitnis, V. R. 2021, MNRAS, 504, 1103, doi: [10.1093/mnras/stab975](https://doi.org/10.1093/mnras/stab975)

Rybicki, G. B., & Lightman, A. P. 1979, Radiative processes in astrophysics

Schmidt, G. D., Stockman, H. S., & Smith, P. S. 1992, ApJL, 398, L57, doi: [10.1086/186576](https://doi.org/10.1086/186576)

Shakura, N. I., & Sunyaev, R. A. 1973, A&A, 24, 337

Shaw, M. S., Romani, R. W., Cotter, G., et al. 2012, ApJ, 748, 49, doi: [10.1088/0004-637X/748/1/49](https://doi.org/10.1088/0004-637X/748/1/49)

Smith, P. S., Montiel, E., Rightley, S., et al. 2009, arXiv e-prints, arXiv:0912.3621, doi: [10.48550/arXiv.0912.3621](https://doi.org/10.48550/arXiv.0912.3621)

Urry, C. M., & Padovani, P. 1995, PASP, 107, 803, doi: [10.1086/133630](https://doi.org/10.1086/133630)

Virtanen, P., Gommers, R., Oliphant, T. E., et al. 2020, Nature Medicine, 17, 261, doi: [10.1038/s41592-019-0686-2](https://doi.org/10.1038/s41592-019-0686-2)

Wang, C.-Z., & Jiang, Y.-G. 2024, ApJ, 966, 65,

doi: [10.3847/1538-4357/ad2fc7](https://doi.org/10.3847/1538-4357/ad2fc7)

Wang, J.-T., & Jiang, Y.-G. 2025, MNRAS, 536, 1251,

doi: [10.1093/mnras/stae2609](https://doi.org/10.1093/mnras/stae2609)

Welsh, W. F. 1999, PASP, 111, 1347, doi: [10.1086/316457](https://doi.org/10.1086/316457)

Woo, J.-H., & Urry, C. M. 2002, ApJ, 579, 530, doi: [10.1086/342878](https://doi.org/10.1086/342878)

Woo, J.-H., Yoon, Y., Park, S., Park, D., & Kim, S. C. 2015, ApJ, 801, 38, doi: [10.1088/0004-637X/801/1/38](https://doi.org/10.1088/0004-637X/801/1/38)

Xie, G. Z., Liu, H. T., Cha, G. W., et al. 2005, AJ, 130, 2506, doi: [10.1086/497163](https://doi.org/10.1086/497163)

Zhang, Z.-X., Du, P., Smith, P. S., et al. 2019, ApJ, 876, 49, doi: [10.3847/1538-4357/ab1099](https://doi.org/10.3847/1538-4357/ab1099)

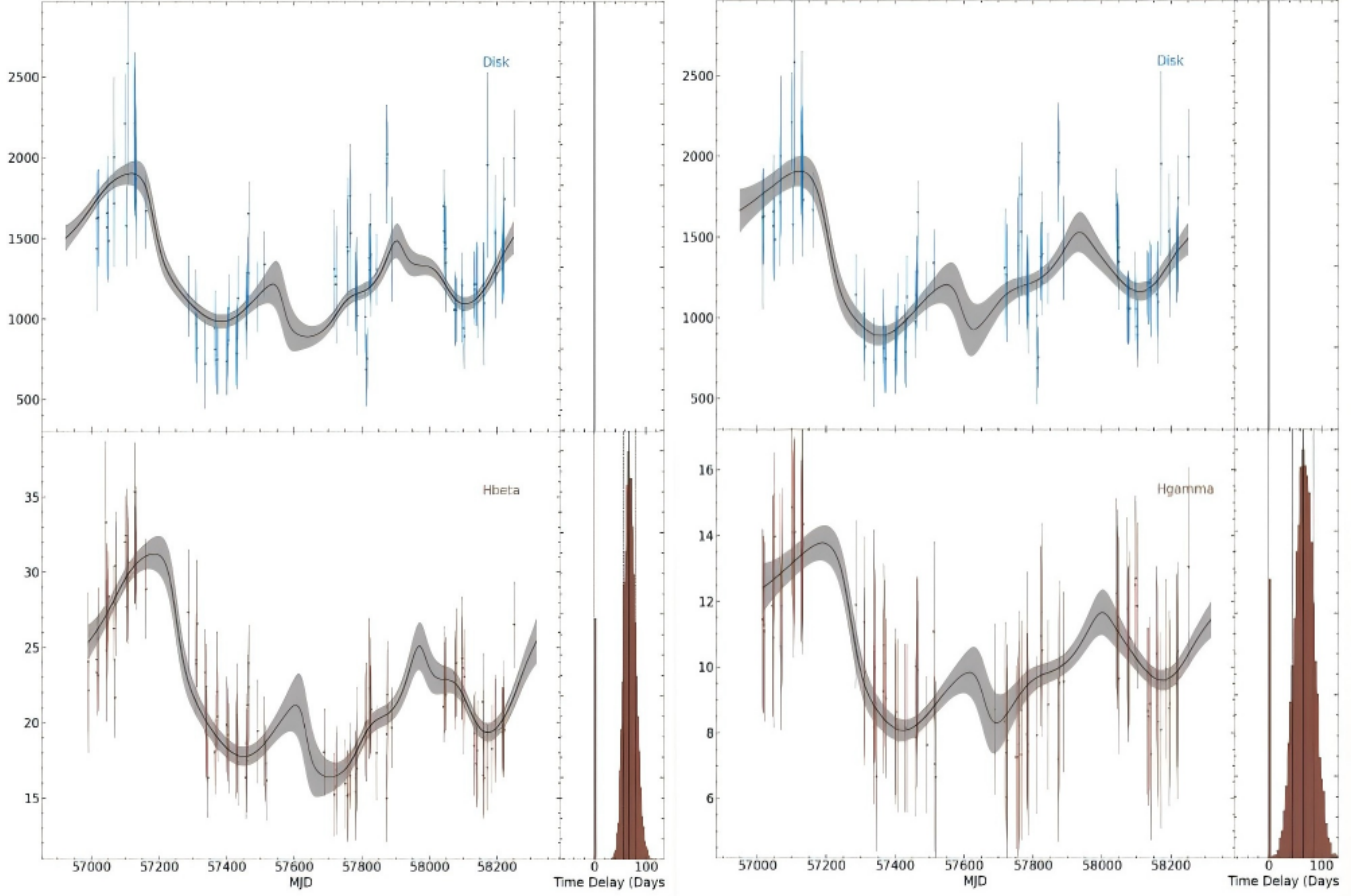


Figure A4. The figure shows the PyROA output for PKS 0736+017. The left panel displays the result between the disk and the $H\beta$ line, while the right panel shows the result with the $H\gamma$ line.